

Article

Mechanism Analysis of a Subsequent Commutation Failure and a DC Power Recovery Speed Control Strategy

Bowen Zheng, Jiawei Hu, Tong Wang * and Zengping Wang

State Key Laboratory of Alternate Electrical Power System with Renewable Energy Sources, North China Electric Power University, Beijing 102206, China; zhengbowen@ncepu.edu.cn (B.Z.); hjwjh12@gmail.com (J.H.); wangzp@ncepu.edu.cn (Z.W.)

* Correspondence: hdwangtong@ncepu.edu.cn; Tel.: +86-134-0111-7137

Abstract: A subsequent commutation failure (SCF) of the Line-Commutated Converter–High-Voltage Direct Current (LCC-HVDC) may occur during the recovery after the clearance of an AC fault, seriously threatening the safe and stable operation of the LCC-HVDC and the entire post-fault AC/DC hybrid power system. In this study, the mechanism of an SCF as affected by the transient stability was analyzed, and a DC power recovery speed control strategy is proposed as an additional form of control to prevent the occurrence of SCFs. First, the sending-end and receiving-end power systems were modeled as synchronous generators instead of ideal voltage sources, and the mechanism of an SCF as affected by the transient stability was analyzed and verified. Second, the ramp function was adopted to describe the recovery characteristic of DC power, and a model of its recovery was established. Then, the recovery speed control strategy is presented based on the mechanism analysis of SCFs, which can not only be used to avoid the occurrence of SCFs but also increase the transient stability margin of the sending-end power system. Finally, the effectiveness and robustness of the proposed control strategy were validated by using a hybrid electromechanical–electromagnetic model and the full electromagnetic model of the IEEE 39-bus asynchronous interconnection test power system. With the implementation of the proposed control strategy, the safe and stable operation of the LCC-HVDC and AC/DC hybrid power system can be guaranteed. The adaptive DC power recovery speed control strategy will be further investigated in future research work.

Keywords: subsequent commutation failure; transient stability; mechanism analysis; recovery speed control strategy; safe and stable operation



Citation: Zheng, B.; Hu, J.; Wang, T.; Wang, Z. Mechanism Analysis of a Subsequent Commutation Failure and a DC Power Recovery Speed Control Strategy. *Electronics* **2022**, *11*, 998. <https://doi.org/10.3390/electronics11070998>

Academic Editor: Adel M. Sharaf

Received: 18 February 2022

Accepted: 20 March 2022

Published: 23 March 2022

Publisher's Note: MDPI stays neutral with regard to jurisdictional claims in published maps and institutional affiliations.



Copyright: © 2022 by the authors. Licensee MDPI, Basel, Switzerland. This article is an open access article distributed under the terms and conditions of the Creative Commons Attribution (CC BY) license (<https://creativecommons.org/licenses/by/4.0/>).

1. Introduction

For the purpose of optimizing the energy structure and resource allocation, promoting the consumption of new sources of energy, such as wind power [1], and reducing carbon emissions [2], Line-Commutated Converter–High-Voltage Direct Current (LCC-HVDC) transmission technology has been rapidly developed due to its advantages in long-distance bulk power transmission and the interconnection of regional power grids [3]. Differently from fully controlled power electronic devices such as Insulated Gate Bipolar Transistors (IGBTs) [4], the thyristors adopted by LCC-HVDC are semi-controlled power electronic devices. Consequently, an inverter bus voltage is needed for the commutation process between the thyristor-based valves, and a deterioration in the inverter bus voltage will lead to the occurrence of a commutation failure (CF) of the LCC-HVDC [5]. In addition, CFs and the DC power fluctuations caused by CFs will bring about new challenges to the safe and stable operation of LCC-HVDC and AC/DC hybrid power systems [6].

The first commutation failure (CF) is unavoidable, and a subsequent commutation failure (SCF) may occur when an AC fault occurs in the receiving-end power system [7]. An SCF of the LCC-HVDC will not only cause overcurrent issues with the converter valves, resulting in the shortening of their service life [8], but also severe DC power fluctuations in

a short period of time [9], seriously threatening the transient stability of the sending-end power system [10]. Additionally, an SCF may occur during the AC fault [11] or during the recovery after the clearance of the AC fault [12]. Moreover, an SCF may occur due to another AC fault, such as a cascading failure or a reclosure on a permanent AC fault [13]. Therefore, SCFs are divided into Category 1, Category 2, and Category 3 SCFs. The occurrence mechanisms of the three categories of SCFs are not the same, so the prevention control strategies are different.

Category 3 SCFs can only be prevented by avoiding the occurrence of a cascading failure [14] or adopting adaptive reclosing instead of the DC control system itself [15].

Regarding Category 1 SCFs, the mechanism of an SCF as affected by improper interactions between DC controllers was deeply analyzed in [11], and the recovery control strategy of an adaptive extinction angle was employed to avoid the occurrence of SCFs. The recovery performance of a CF was improved in order to prevent the occurrence of SCFs by modifying the lower and upper limits of a Constant Extinction Angle (CEA) controller in [16]. Based on an analysis of the controller response and AC/DC interaction, an early warning system for SCFs was developed by considering the risks of controller regulation and the variations in electrical quantities in [17,18], and an emergency advanced control strategy was proposed with an adjustment of the inverter beta in [17]. In addition, the impact of the conventional Phase-Locked Loop (PLL) on SCFs during an AC fault was analyzed. In [19], a novel PLL was presented that supplies a precise phase reference for the DC control system, thereby reducing the probability of SCFs. The output of the extinction angle or DC voltage control was modified to mitigate the SCF by taking the error between the AC voltage phase and the PLL's output angle into account in [20]. Moreover, in order to inhibit the SCF during an AC fault, a Commutation Failure Inhibition Module (CFIM) with a high response speed was designed in order to modify the firing angle by direct measurement of the overlapping area in [7]. A Controllable Commutation Failure Inhibitor (CCFI) was established in order to make the fault current rely on a reduced extinction angle in [21].

Category 2 SCFs are mainly related to the inverter bus voltage during the recovery after the clearance of an AC fault. On the one hand, by installing a Static Var Compensator (SVC) [22], the inverter bus voltage can be effectively supported during the recovery after the clearance of the AC fault, which will reduce the probability of SCFs, but additional investment is required. On the other hand, the DC control system could be optimized in order to prevent the occurrence of SCFs. In [23], an adaptive Voltage-Dependent Current Order Limiter (VDCOL) based on granular computing and fuzzy rules was applied to lower the reactive power consumption during low-voltage periods. In [12], the VDCOL was replaced with a novel current order control strategy on the basis of the relationship between the DC current order, the inverter bus voltage, and the inverter reactive power in order to improve the recovery performance.

In the above-mentioned studies on the mechanisms and prevention control strategies of SCFs, due to the fact that scholars have mainly focused on the LCC-HVDC itself, and not on the entire AC/DC hybrid power system, almost all receiving-end power systems are modeled as ideal voltage sources instead of synchronous generators, so the dynamic interaction characteristics between the AC system and the DC system are neglected. However, from the perspective of an AC/DC hybrid power system, the fluctuation in the DC power caused by the SCF has negative impact on the transient stability of the post-fault AC/DC hybrid power system, and the deterioration of the transient stability also affects the inverter bus voltage, which may cause additional SCFs to occur. Therefore, the sending-end and receiving-end power systems should be modeled as synchronous generators instead of ideal voltage sources. As a result, the mechanism of an SCF as affected by the transient stability can be analyzed and a corresponding control strategy can be proposed in order to prevent the occurrence of SCFs and guarantee the safe and stable operation of the LCC-HVDC and AC/DC hybrid power system.

In Section 2, the three categories of SCFs and their impacts on transient stability are further discussed. In Section 3, the mechanism of an SCF as affected by transient stability is analyzed based on the transient stability of the receiving-end power system and the reactive power characteristics of the inverter station and then validated by simulation results. In Section 4, a DC power recovery model is established by adopting the ramp function, and a recovery speed control strategy is presented that can be used to not only avoid the occurrence of SCFs but also increase the transient stability margin of the sending-end power system. In Section 5, a hybrid electromechanical–electromagnetic model and the full electromagnetic model of the IEEE 39-bus asynchronous interconnection test power system are adopted to confirm the effectiveness and robustness, respectively, of the proposed control strategy. Section 6 concludes this paper.

2. Definition of an SCF

The commutation process in an inverter station can be represented in the following manner [24]:

$$\gamma = (\pi - \alpha_I) - \mu = \beta - \mu \quad (1)$$

where α_I is the firing angle, β is the advanced firing angle, μ is the commutation angle, and γ is the extinction angle.

During the operation of the inverter, when the time (extinction angle γ) of application of negative voltage to the thyristor that has just been turned off is shorter than the time (inherent extinction angle γ_{\min}) required for it to restore the blocking capability and the thyristor is turned on again when positive voltage is applied, a commutation failure of the inverter will occur, and the occurrence of repeated commutation failures in a short period of time is called an SCF. The SCF may occur during an AC fault or occur during the recovery after the clearance of an AC fault. In addition, an SCF may occur due to another AC fault, such as a cascading failure or a reclosure on a permanent AC fault. Therefore, SCFs are divided into three categories according to the occurrence time of the SCF and the AC fault conditions. Definitions for the three categories of SCFs are given below.

Category 1: The AC fault occurs in the receiving-end power system, causing the occurrence of the first CF. The SCF occurs during the recovery when the AC fault has not yet been cleared.

Category 2: The AC fault occurs in the receiving-end power system, causing the occurrence of the first CF. The SCF occurs during the recovery after the clearance of the AC fault.

Category 3: The first CF and the SCF are caused by multiple AC faults, such as a cascading failure or a reclosure on a permanent AC fault. The first and second AC faults cause the occurrence of the first CF and the SCF, respectively.

Regarding the transient stability analysis, we are most concerned with the external characteristics of converter stations, especially DC power. The simulation results of SCFs corresponding to the three categories are shown in Figure 1.

As shown in Figure 1a, the fault duration is the same, but the fault types are a single-phase resistance grounding fault and a three-phase short circuit fault, respectively. It can be seen from Figure 1aI that the SCF corresponding to Category 1 does not have a significant negative impact on the DC power during the AC fault. In contrast, it can be seen from Figure 1a (the red dotted line) and (b) that the SCFs corresponding to Category 2 and Category 3 cause severe fluctuations in the DC power and seriously affect the transient stability of the power system. To sum up, the order of the impact of the SCFs on the transient stability is Category 3 > Category 2 > Category 1. Next, we discuss the SCFs corresponding to Category 2.

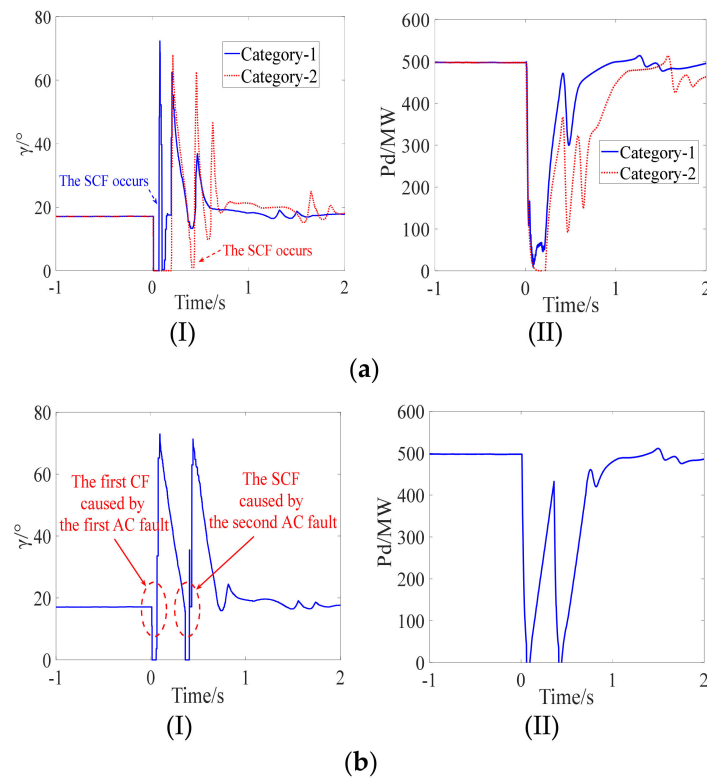


Figure 1. Simulation results of SCFs. (a) SCF corresponding to Category 1 and Category 2, (I) Extinction angle and (II) DC power; (b) SCF corresponding to Category 3, (I) Extinction angle and (II) DC power.

3. Mechanism Analysis of an SCF

There is a high probability that an SCF as affected by transient stability will occur when the transient stability of the receiving-end power system has seriously deteriorated. The deterioration of the transient stability will affect the support capability of the inverter bus voltage during the recovery after the clearance of the AC fault and indirectly affect the reactive power recovery characteristics, resulting in the occurrence of a Category 2 SCF.

3.1. Impact of the Transient Stability of a Post-Fault Receiving-End Power System on an SCF

An equivalent model of the receiving-end power system was established and is shown in Figure 2 [25].

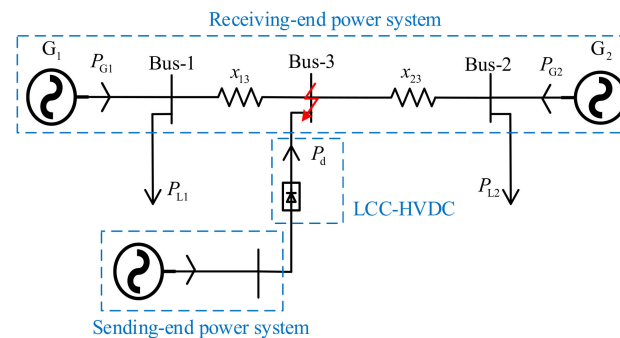


Figure 2. Equivalent model of the receiving-end power system.

An infinite model of the single machine can be obtained as follows:

$$M_{eq} \frac{d^2 \delta}{dt^2} = P_M - P_E \tag{2}$$

$$M_{eq} = \frac{M_1 M_2}{M_1 + M_2} \tag{3}$$

$$P_M = \frac{1}{M_1 + M_2} (M_2 P_{m1} - M_1 P_{m2}) \tag{4}$$

$$P_E = \frac{1}{M_1 + M_2} (M_2 P_{e1} - M_1 P_{e2}) \tag{5}$$

where P_{m1} and P_{m2} are the mechanical power of G_1 and G_2 , respectively; P_{e1} and P_{e2} are the electromagnetic power of G_1 and G_2 , respectively; M_1 and M_2 are the inertia constant of G_1 and G_2 , respectively; and δ_1 and δ_2 are the rotor angle of G_1 and G_2 , respectively.

$$\begin{cases} \int_{\delta(0)}^{\delta(t_c)} d\delta = \int_0^{t_c} \frac{P_M}{M_{eq}} dt \\ \int_{\delta(0)}^{\delta(t_c)} d\delta = \int_0^{t_c} \frac{P_M}{M_{eq}} t dt \\ \delta(t_c) = \delta(0) + \frac{1}{2} \frac{P_M}{M_{eq}} t_c^2 \end{cases} \tag{6}$$

A three-phase short-circuit fault was set at the Bus-3 inverter bus and the fault duration is t_c , so $P_E = 0$ for the duration of the fault. Then, the relative rotor angle $\delta(t_c)$ of the receiving-end power system at t_c can be derived based on Equation (6).

Assuming that the internal electromotive force of G_1 and G_2 is $U_1 \angle \delta(t_c)$ and $U_2 \angle 0^\circ$, respectively, the AC that is fed into the receiving-end power system by the inverter station is I_{i-ac} , and the internal impedance and the load of generators are ignored, the equation for the relationship between the voltage U_3 of the inverter bus and the relative rotor angle $\delta(t_c)$ of the receiving-end power system can be derived based on the superposition theorem as follows.

$$\begin{aligned} \dot{U}_3 &= \frac{x_{23}}{x_{13} + x_{23}} \dot{U}_1 + \frac{x_{13}}{x_{13} + x_{23}} \dot{U}_2 + \frac{x_{13} x_{23}}{x_{13} + x_{23}} \dot{I}_{i-ac} \\ &= \dot{U}_{31} + \frac{x_{13} x_{23}}{x_{13} + x_{23}} \dot{I}_{i-ac} \end{aligned} \tag{7}$$

$$U_{31}^2 = \frac{x_{13}^2 U_2^2 + x_{23}^2 U_1^2}{(x_{13} + x_{23})^2} + \frac{2x_{13} x_{23} U_1 U_2}{(x_{13} + x_{23})^2} \cos \delta(t_c) \tag{8}$$

where x_{12} and x_{23} are the reactance between Bus-1 and Bus-2 and Bus-2 and Bus-3, respectively.

It can be seen from Equations (6)–(8) that the longer the fault lasts, the larger the relative rotor angle of the post-fault receiving-end power system is, and the weaker the support capability of the inverter bus voltage will be, resulting in a higher probability of the occurrence of an SCF. The above conclusions were verified by the AC/DC asynchronous interconnection power system shown in Figure 2. The simulation results are shown in Figure 3.

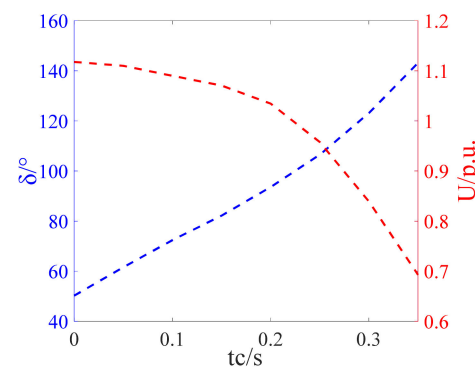


Figure 3. Simulation results of the receiving-end power system.

3.2. Impact of Reactive Power Characteristics of the Inverter Station on an SCF

The reactive power exchange characteristics between the inverter station and the receiving-end power system are given in Figure 4 [26].

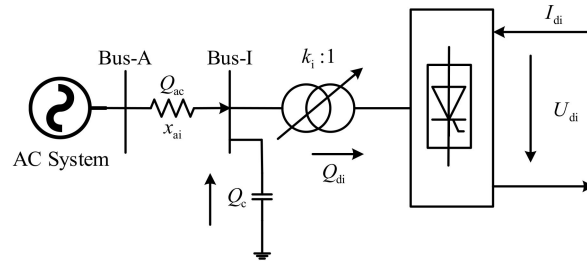


Figure 4. Equivalent model of the inverter station.

The following equation can be obtained from Figure 5.

$$Q_{ac} = Q_{di} - Q_c \tag{9}$$

where Q_{ac} is the reactive power flowing from the receiving-end power system to the inverter station, Q_c is the reactive power generated by the reactive power compensation equipment at the inverter bus, and Q_{di} is the reactive power expended by the inverter station.

It can be further seen from Figure 5 that

$$\dot{U}_{LI} = \dot{U}_A - d\dot{U} = \dot{U}_A - \Delta U - j\Delta U' \tag{10}$$

where U_{LI} is the voltage of Bus-I and U_A is the voltage of Bus-A.

Equation (11) can be deduced by ignoring the line resistance and $\Delta U'$ on the basis of Equations (9) and (10).

$$U_{LI} = U_A - \frac{Q_{ac}x_{ai}}{U_{LI}} = U_A - \frac{(Q_{di} - Q_c)x_{ai}}{U_{LI}} \tag{11}$$

where x_{ai} is the reactance between Bus-I and Bus-A.

In addition, the reactive power Q_{di} expended by the inverter side can be represented by:

$$\begin{aligned} Q_{di} &= P_{di} \tan \varphi_i = P_{di} \tan \left(\arccos \left(\frac{U_{di}}{U_{di0}} \right) \right) \\ &= U_{di} I_{di} \frac{\sqrt{U_{di0}^2 - U_{di}^2}}{U_{di}} = I_{di} \sqrt{U_{di0}^2 - U_{di}^2} \\ &= I_{di} \sqrt{\left(\frac{3\sqrt{2}}{\pi} k_i N_p U_{LI} \right)^2 - \left(\frac{3\sqrt{2}}{\pi} k_i N_p U_{LI} \cos \gamma - \frac{3}{\pi} x_{ci} I_{di} \right)^2} \end{aligned} \tag{12}$$

where U_{di} is the DC voltage, U_{di0} is the ideal no-load DC voltage, I_{di} is the DC current, P_{di} is the DC power, φ_i is the power factor, x_{ci} is the commutation reactance, N_p represents the number of poles, and k_i represents the ratio of the converter transformer.

Finally, the partial derivative of U_{LI} and I_{di} can be deduced as follows:

$$\frac{\partial U_{LI}}{\partial I_{di}} = \frac{\partial U_{LI}}{\partial Q_{di}} \frac{\partial Q_{di}}{\partial I_{di}} < 0 \tag{13}$$

It can be further seen from Equation (13) that the inverter bus voltage U_{LI} will decrease with an increase in the DC current I_{di} . In conclusion, the probability of the occurrence of an SCF will greatly increase due to the larger increase in the DC current when the switching of inverter controllers occurs during the recovery after the clearance of the AC fault.

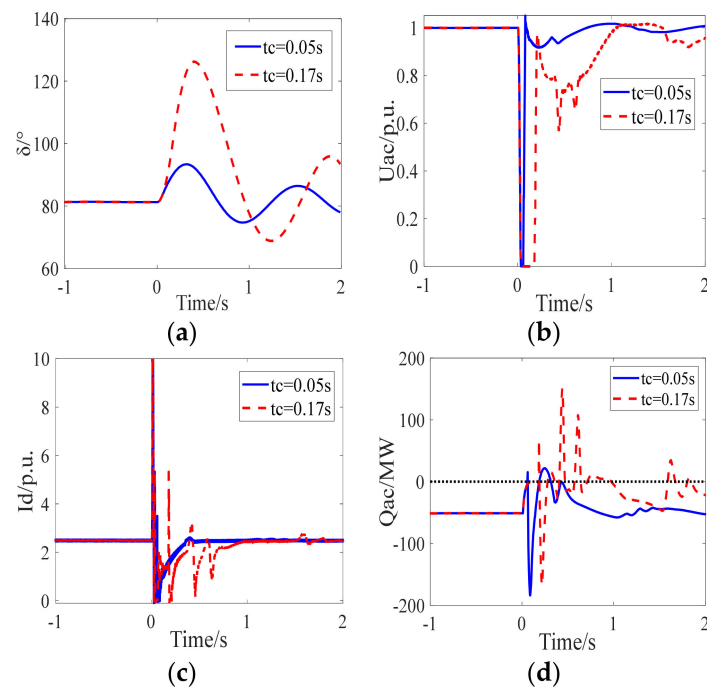


Figure 5. Comparison of the results of simulations with different fault durations. (a) Relative rotor angle, (b) inverter bus voltage, (c) DC current, and (d) reactive power.

3.3. Simulation Verification

A three-phase short circuit fault was set at the inverter bus in the AC/DC asynchronous interconnection power system, and the fault durations were $t_c = 0.05$ s and $t_c = 0.17$ s, respectively. A comparison of the simulation results is shown in Figure 6, which verifies the correctness of the mechanism analysis for SCFs as affected by transient stability.

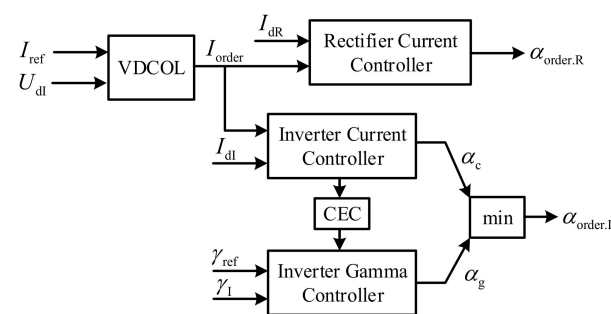


Figure 6. DC control system.

As shown in Figure 5a,b, the relative rotor angle of the receiving-end power system is larger when the fault duration increases, resulting in a decrease in the support capability of the inverter bus voltage based on Equation (8). Furthermore, it can be seen from the red dotted line shown in Figure 5c that the DC current increases rapidly when the DC controllers switch during the recovery. The reason for this is that the support capability of the inverter bus voltage is weak while the recovery level of the DC current is relatively high. Then, based on Equation (12), the reactive power expended by the inverter side increases significantly, causing the reactive power to flow in the reverse direction between the inverter station and the receiving-end power system and further weakening the support capability of the inverter bus voltage (based on Equation (13)) as shown in Figure 5d. As a result, an SCF as affected by the transient stability occurs during the recovery after the clearance of the AC fault, causing a severe fluctuation in the DC power.

Next, we discuss the rapid increase in the DC current caused by the switching of DC controllers during the recovery. The DC control system based on the Cigre Benchmark model of LCC-HVDC is given in Figure 6 [27].

The simulation results of the inverter side during the recovery are shown in Figure 7.

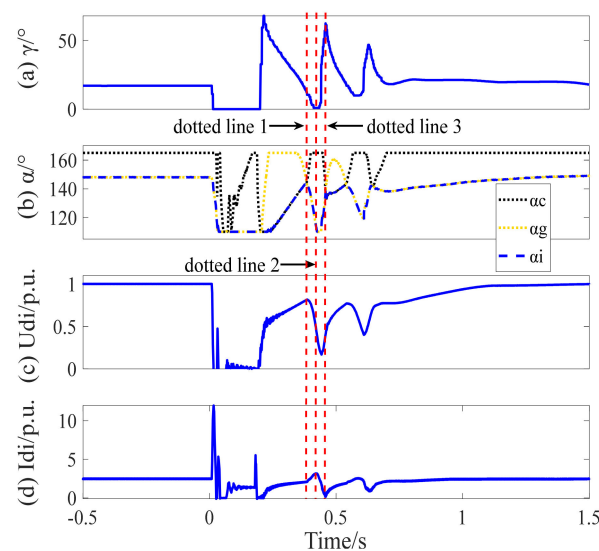


Figure 7. Simulation results of the DC control system. (a) Extinction angle, (b) Outputs of inverter controllers, (c) DC voltage, and (d) DC current.

In Figure 7a, the blue solid line depicts the extinction angle of the inverter station. In Figure 7b, the black, yellow, and blue dotted lines depict the firing angle output of the inverter current controller, the inverter gamma controller, and the inverter control system, respectively. In Figure 7c, the blue solid line depicts the DC voltage of the inverter station. In Figure 7d, the blue solid line depicts the DC current of the inverter station.

It can be seen from Figure 7b that the DC controllers switch during the recovery. At the first red dotted line, the inverter control system switches from the inverter current controller to the inverter gamma controller. Then, the firing angle of the inverter station begins to decrease. Therefore, the DC voltage of the inverter station decreases, causing an increase in the DC voltage difference between the rectifier side and the inverter side. Meanwhile, the DC current increases quickly within a very short period of time and reaches the maximum value at the second red dotted line. During the period between the first red dotted line and the second red dotted line, the rapid increase in the DC current causes an increase in the reactive power consumption of the inverter station and a decrease in the inverter bus voltage. Then, the DC current begins to decrease with the regulation of the rectifier current controller, while the extinction angle of the inverter station begins to increase as shown in Figure 7a,c,d. At the third red dotted line, the inverter control system switches from the inverter gamma controller to the inverter current controller and finally enters into a normal state of operation with the regulation of the inverter gamma controller.

In conclusion, the rapid increase in the DC current caused by the switching of DC controllers cannot be avoided during the recovery after the clearance of the AC fault, and the increase in the amplitude of the DC current differs. The amplitude of the DC current will greatly increase when the support capacity of the inverter bus voltage is weak due to the deterioration of the transient stability of the receiving-end power system and the recovery level of the DC current is relatively high, resulting in the occurrence of an SCF as affected by transient stability. Therefore, it is essential to limit the recovery speed in order to prevent the occurrence of Category 2 SCFs when the transient stability of the receiving-end power system has seriously deteriorated. Moreover, the transient stability margin of the sending-end power system can be increased by avoiding the severe fluctuation in the DC power that is caused by an SCF.

4. Derivation of a Prevention Control Strategy for Category 2 SCFs

In this section, a DC power recovery speed control strategy is proposed as an additional form of control to prevent the occurrence of Category 2 SCFs. In order to determine whether an SCF will occur during the recovery after the clearance of an AC fault, a risk assessment index for SCFs is deduced based on a quasi-steady-state model of the DC control system. A DC power recovery model is then established based on the ramp function, and the impact of DC controller parameters on the DC power recovery speed is analyzed. Finally, the DC power recovery speed control strategy is used to limit the recovery speed by modifying the output DC current order to prevent the occurrence of the SCF once the risk of it occurring during the recovery after the clearance of the AC fault has been assessed.

4.1. Risk Assessment of SCFs

When the AC fault is removed, the DC system recovers steadily with the regulation of the DC controllers. According to the mechanism analysis presented in Section 3, the SCFs as affected by transient stability mainly occur in the middle period or the later period of the recovery after the clearance of the AC fault. In order to simplify the derivation process, the quasi-steady-state model of the DC control system was employed to deduce the risk assessment index for SCFs.

The quasi-steady-state model of the DC control system can be represented by

$$\begin{cases} U_{dr} = N_p (U_{dr0} \cos \alpha - I_d \frac{3}{\pi} x_{cr}) \\ U_{dr0} = \frac{3\sqrt{2}}{\pi} k_r U_{LR} \\ U_{di} = N_p (U_{di0} \cos \gamma - I_d \frac{3}{\pi} x_{ci}) \\ U_{di0} = \frac{3\sqrt{2}}{\pi} k_i U_{LI} \\ I_d = (U_{dr} - U_{di}) / R_l \end{cases} \quad (14)$$

where U_{dr} and U_{di} represent the DC voltage on the rectifier side and the inverter side, respectively, U_{dr0} and U_{di0} are the ideal no-load DC voltage of the rectifier and the inverter, respectively, I_d is the DC current, R_l is the resistance of the DC line, x_{cr} and x_{ci} are the commutation reactance of the rectifier and the inverter, respectively, and k_r and k_i are the ratio of the converter transformer of the rectifier and the inverter, respectively.

Moreover, U_{di} can be represented by

$$U_{di} = N_p U_{di0} \frac{(\cos \gamma + \cos \beta)}{2} \quad (15)$$

Based on Equations (14) and (15), we can obtain:

$$U_{LImin} = \frac{\sqrt{2} I_d x_{ci}}{k_i (\cos \gamma_{min} - \cos \beta)} \quad (16)$$

Then, I_d can be rewritten in the following manner.

$$\begin{cases} I_d = N_p (U_{dr0} \cos \alpha - U_{di0} \cos \gamma) / (N_p R_{cr} + R_l + N_p R_{ci}) \\ R_{cr} = \frac{3}{\pi} x_{cr} \\ R_{ci} = \frac{3}{\pi} x_{ci} \end{cases} \quad (17)$$

where $N_p R_{cr}$ and $N_p R_{ci}$ are the equivalent resistance of the rectifier station and the inverter station, respectively.

Equation (18) was derived based on Equations (16) and (17).

$$U_{LImin} = \frac{\sqrt{2} x_{ci} N_p U_{dr0} \cos \alpha}{k_i ((R_{cr} + R_l + R_{ci}) (\cos \gamma_{min} - \cos \beta) + \frac{6}{\pi} x_{ci} N_p \cos \gamma_{min})} \quad (18)$$

There is a high risk of the occurrence of an SCF when $U_{LI} < U_{LImin}$ during the recovery after the clearance of the AC fault, and the proposed control strategy should be enabled when Equation (19) is satisfied.

$$U_{LI} < U_{LImin} = \zeta_1 U_{LLe}, t > t_c \tag{19}$$

where U_{LLe} is the rated inverter bus voltage and ζ_1 is the threshold coefficient.

In addition, the enabling criterion was further improved in order to avoid the impact of the deterioration of the inverter bus voltage caused by harmonics during the early period of recovery.

$$U_{LI} < \zeta_1 U_{LLe}, t > t_c + 3T_e \tag{20}$$

where $T_e = 1/f_e = 0.02$ s.

4.2. Recovery Speed Control Strategy

According to the mechanism analysis presented in Section 3, the recovery speed of the DC control system can be limited in order to prevent the occurrence of an SCF when there is a risk that an SCF will occur during the recovery after the clearance of the AC fault. Therefore, DC power recovery speed control is investigated in this paper. According to the external features of the inverter station, a recovery model of DC power was built, which is shown as the blue solid line in Figure 8. The ramp function was employed to describe the recovery characteristic of DC power as given in Equation (21).

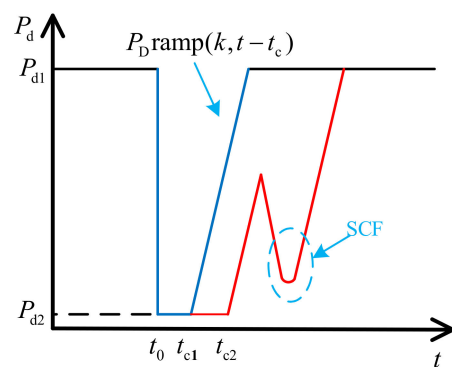


Figure 8. DC power recovery speed model.

According to the presented mechanism analysis of an SCF as affected by the transient stability of the receiving-end power system, the longer the fault clearing time t_c is, the lower the transient stability of the receiving-end power system will be, resulting in a weakening of the inverter bus voltage’s support capability. Consequently, an SCF will occur during the recovery after the clearance of the AC fault, which is shown as the red solid line in Figure 8. It is essential to limit the recovery speed in the DC control system when the transient stability of the receiving-end power system has seriously deteriorated. Therefore, a DC power recovery speed control strategy is proposed in order to avoid the occurrence of an SCF as affected by transient stability.

$$P_d = \begin{cases} P_{d1} & t_0 < t \\ P_{d2} & t_0 < t < t_c \\ P_{d2} + P_D \text{ramp}(k, t - t_c) & t_c < t \end{cases} \tag{21}$$

where k is the recovery speed of DC power.

When the AC fault is cleared, the Voltage-Dependent Current Limit Control (VDCOL) limits the DC current according to the DC voltage level during the recovery, thereby affecting the recovery speed of DC power. A mathematical model of the VDCOL is given in Figure 9, where U_{di} is the DC voltage, T_{in} is the time constant of the filter loop, U_{dlow}

is the start voltage, U_{dhigh} is the exit voltage, I_{omin} is the minimum current order, I_o is the rated DC current, and I_{olim} is the output DC current order [28].

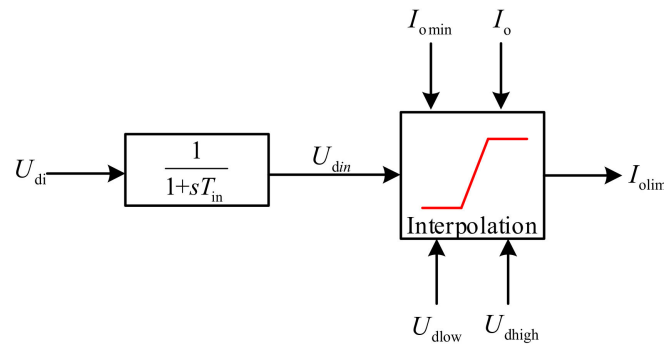


Figure 9. Mathematical model of the VDCOL.

It can be seen from Figure 9 that the output relationship of the VDCOL can be deduced in the following manner.

$$U_{di} = \frac{3\sqrt{2}}{\pi} k_i N_p U_{LI} \cos \gamma - \frac{3}{\pi} x_{ci} I_{di} \tag{22}$$

$$U_{din} = U_{di} \left(1 - e^{-\frac{t}{T_{in}}} \right) \tag{23}$$

$$I_{olim} = \begin{cases} I_{omin} & U_{din} < U_{dlow} \\ I_{omin} + \frac{I_o - I_{omin}}{U_{dhigh} - U_{dlow}} (U_{din} - U_{dlow}) & U_{dlow} < U_{din} < U_{dhigh} \\ I_o & U_{dhigh} < U_{din} \end{cases} \tag{24}$$

Assuming that the commutation loss is ignored and the VDCOL is ideal, i.e., $I_{di} = I_{olim}$ during the recovery, the DC power P_{di} fed into the receiving-end power system through the inverter station can be represented by

$$P_{di} = U_{di} \cdot I_{olim} \tag{25}$$

Then, the recovery speed k of DC power can be obtained by deriving DC power P_{di} with respect to time t .

$$k = U'_{di} \left(I_{omin} + \frac{I_o - I_{omin}}{U_{dhigh} - U_{dlow}} (2U_{din} - U_{dlow}) \right) + \frac{(I_o - I_{omin}) U_{di}^2}{(U_{dhigh} - U_{dlow}) T_{in}} e^{-\frac{t}{T_{in}}} \tag{26}$$

Finally, the partial derivative of k with respect to the control parameter I_o can be derived as follows.

$$\frac{\partial k}{\partial I_o} = U'_{di} \frac{2U_{din} - U_{dlow}}{U_{dhigh} - U_{dlow}} + \frac{U_{di}^2}{(U_{dhigh} - U_{dlow}) T_{in}} e^{-\frac{t}{T_{in}}} > 0 \tag{27}$$

It can be seen from Equation (27) that the recovery speed k of the DC power is proportional to the control parameter I_o of the VDCOL, and the DC power recovery speed k can be controlled by modifying I_o . As shown in Figure 10, the larger the I_o is, the faster the recovery speed of the DC power will be, which conforms to the theoretical analysis.

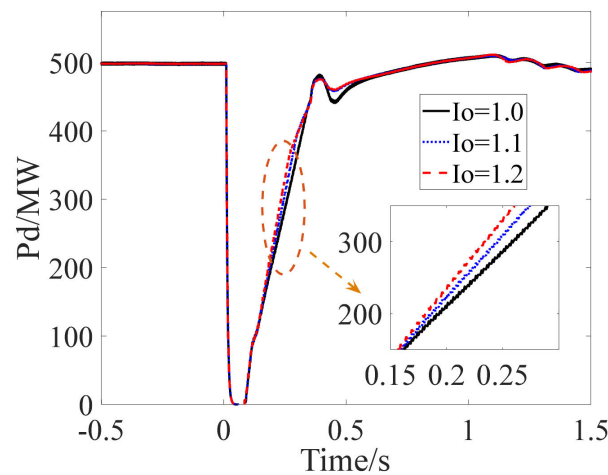


Figure 10. Different I_o values of the VDCOL.

When it is detected that there is a high probability of the occurrence of an SCF based on Equation (20), DC power recovery speed control will be enabled to prevent the occurrence of an SCF. In practice, the control parameter I_o of the VDCOL cannot be modified in real time. Instead, the recovery speed of DC power can be controlled by modifying the output DC current order I_{olim} to be $I'_{olim} = \zeta_2 I_{olim}$ as given in Equation (28).

$$I'_{olim} = \begin{cases} I_{olim} & \text{Enabling criterion} = 0 \\ \zeta_2 I_{olim} & \text{Enabling criterion} = 1 \end{cases} \quad (28)$$

where ζ_2 is a constant coefficient.

Additionally, in order to avoid the severe fluctuation in the DC power caused by disabling the proposed control strategy, the time at which it is disabled must be carefully selected. As shown in Figure 7, the DC current decreases while the extinction angle increases during the period between the second red dotted line and the third red dotted line, indicating that the risk of an SCF occurring is reduced and the proposed control strategy can be disabled at this time. In addition, if the DC power recovery speed control fails when the DC current begins to decrease, the DC current order I'_{olim} will change from $I'_{olim} = \zeta_2 I_{olim}$ to $I'_{olim} = I_{olim}$, which will be larger than the DC current I_{di} at this time, thereby avoiding the decrease in the DC current I_{di} and the severe fluctuation in DC power. The disabling criterion is given in Equation (29), and a time window was added to improve the reliability of the proposed disabling criterion.

$$dI_{di}/dt < 0 \text{ lasts for } T_e/4 \quad (29)$$

In conclusion, when the AC fault is cleared, the DC power recovery speed control will be enabled when a risk that an SCF will occur is detected based on Equation (20). Then, the DC current order output of the VDCOL is modified based on Equation (28) to limit the recovery speed of the DC power, thereby preventing the occurrence of an SCF as affected by transient stability. Then, the proposed control strategy is disabled based on Equation (29) to avoid the DC power fluctuation caused by disabling it. A detailed procedure flowchart for the proposed control strategy is given in Figure 11. In addition, AC fault information can be provided by relay protection devices [29].

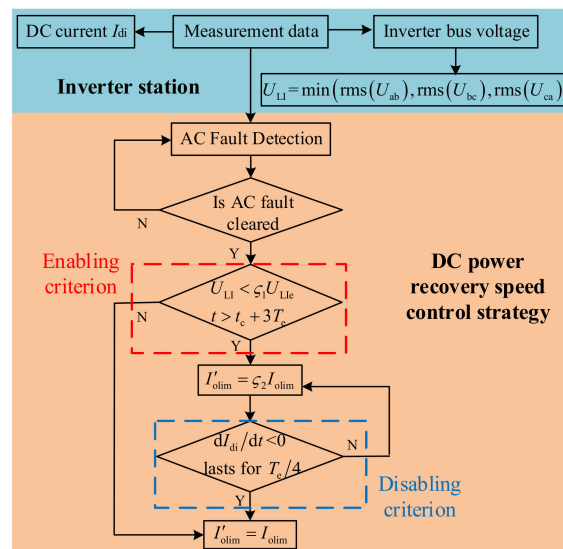


Figure 11. Procedure flowchart for the DC power recovery speed control.

5. Results and Discussion

5.1. Test Power System

A simulation model of the IEEE 39-bus AC/DC asynchronous interconnection power system was built in the Advanced Digital Power System Simulator (ADPSS) to verify the effectiveness and robustness of the DC power recovery speed control strategy presented in this paper. The network topology is given in Figure 12. The AC transmission lines between Bus-1 and Bus-39, and between Bus-3 and Bus-4, were cleared. The AC transmission line between Bus-16 and Bus-17 was replaced by LCC-HVDC, where Bus-16 is the rectifier station bus and Bus-17 is the inverter station bus. The ADPSS was developed by the Chinese Electric Power Research Institute [30] and includes an electromechanical transient simulation module (Power System Analysis Software Package, PSASP) and an electromagnetic transient simulation module (Electromagnetic Transient Simulator for DC and AC power systems, ETSDAC) [31].

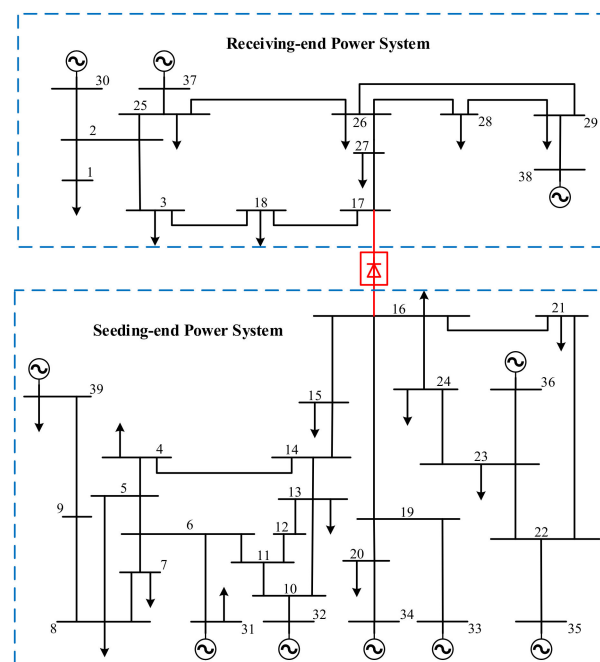


Figure 12. AC/DC asynchronous interconnection power system.

Generally, the time scale of the electromagnetic transient process ranges from microseconds to milliseconds, while the time scale of the electromechanical transient process ranges from milliseconds to seconds. In addition, a commutation failure of LCC-HVDC is an electromagnetic transient process, which requires an electromagnetic model in order to characterize the dynamics of the DC system, while the transient stability of synchronous generators is an electromechanical transient process, which means that the electromechanical model is able to characterize the dynamics of the AC system. The typical simulation steps of the electromagnetic model and the electromechanical model are 50 μ s and 10 ms. Therefore, the DC system adopted the electromagnetic model on ETSDAC, and the AC system adopted the electromechanical model on PSASP. The total simulation time T was 5 s, and the simulation time steps of PSASP and ETSDAC were 10 ms and 50 μ s, respectively. The damping coefficient of the generators was $\mu = D_i/T_{ji}$, and a CF occurred when $\gamma < \gamma_{\min} = 7^\circ$.

As shown in Figure 12, an AC fault was set near the inverter station in the receiving-end power system, and the fault duration was long enough to cause an SCF in the DC system during the recovery after the clearance of the AC fault. Then, the Maximum Relative Rotor Angle (MRRRA) of the generators in the post-fault sending-end power system was employed to assess the transient stability margin, where the generators, except for the generator at Bus-39 (Group B), were grouped into Group A according to the coherence situation when the AC fault occurred. The smaller the relative rotor angle of the post-fault power system during the first swing is, the larger the transient stability margin of the post-fault power system will be.

Finally, two control strategies for the DC control system were defined and employed in different scenarios to verify the effectiveness and robustness of the proposed control strategy.

Control Strategy 1 (CS-1): The DC control system adopts the standard control strategy given in Figure 6.

Control Strategy 2 (CS-2): Based on CS-1, the proposed DC power recovery speed control strategy is employed as an additional form of control by the DC control system. Here, the parameters of the proposed control strategy are $\zeta_1 = 0.9$ and $\zeta_2 = 0.5$.

Scenario 1: A three-phase short circuit fault is set at Bus-17, which starts at $t = 0$ s and lasts for 0.17 s.

The inverter bus voltage, extinction angle, DC power, and relative rotor angle of the sending-end power system are shown in Figure 13a–d. The occurrence of the AC fault causes the first CF of LCC-HVDC. After the clearance of the AC fault, it can be seen from the blue solid line in Figure 13a that the post-fault voltage of the inverter bus decreases rapidly and to a great extent, which indicates that the transient stability of the post-fault receiving-end power system has seriously deteriorated. The SCF (the blue solid line shown in Figure 13b) occurs during the recovery when the DC control system adopts CS-1, demonstrating the correctness of the mechanism analysis of SCFs as affected by transient stability. Moreover, it can be seen from the red dotted line that the SCF is effectively prevented during the recovery when the DC control system adopts CS-2. In CS-2, the proposed control strategy is adopted as an additional form of control. The additional control (the red dotted line shown in Figure 13a) is enabled when Equation (20) is satisfied, while the DC power recovery speed is limited by modifying the output DC current order I_{olim} to $I'_{olim} = \zeta_2 I_{olim}$, so that the occurrence of the SCF is prevented. Then, the additional control is disabled based on Equation (29). Due to the occurrence of the SCF, it can be seen from the blue solid line in Figure 13c that the DC power fluctuates seriously during the recovery. When the proposed control strategy is employed, the recovery characteristic of the DC power is improved, which increases the transient stability margin of the sending-end power system as shown in Figure 13d. The effectiveness of the proposed control strategy is confirmed by the simulation results.

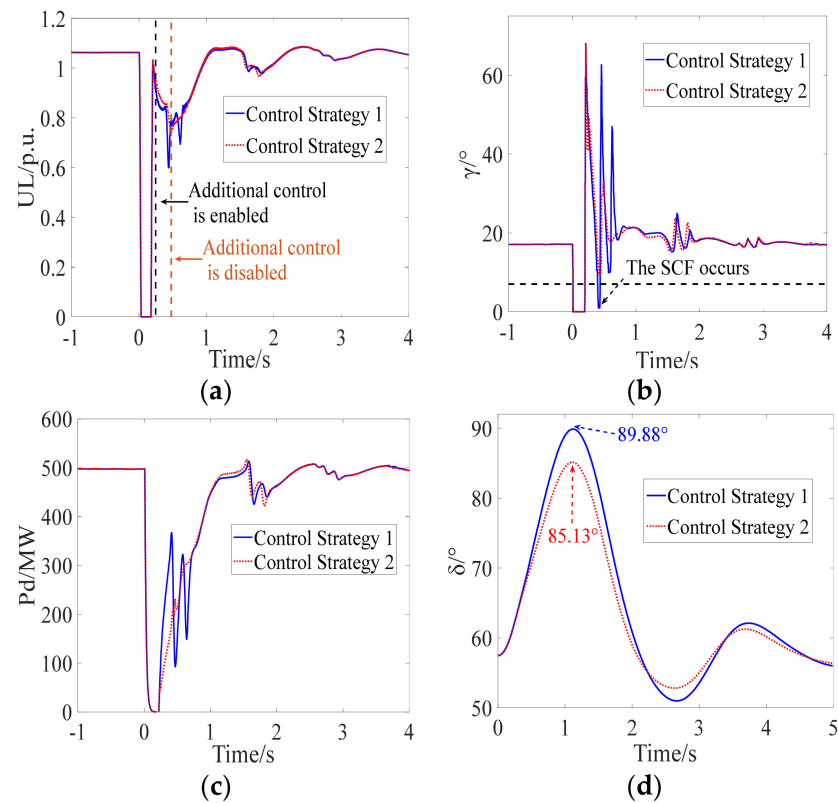


Figure 13. Simulation results of Scenario 1. (a) Inverter bus voltage, (b) extinction angle, (c) DC power, and (d) relative rotor angle.

Scenario 2: A single-phase grounding fault is set at Bus-17, which starts at $t = 0$ s and lasts for 0.36 s.

As shown in Figure 14a,d, the occurrence of the AC fault causes the first CF of LCC-HVDC. After the clearance of the AC fault, an SCF occurs when the DC control system adopts CS-1, while the SCF is prevented when the DC control system adopts CS-2, indicating the effectiveness of the proposed control strategy. As shown Figure 14c,d, the transient stability margin of the sending-end power system is increased due to the fact that the severe fluctuation in DC power caused by an SCF is avoided. A comparison with Scenario 1 verified the effectiveness of the proposed control strategy in different scenarios.

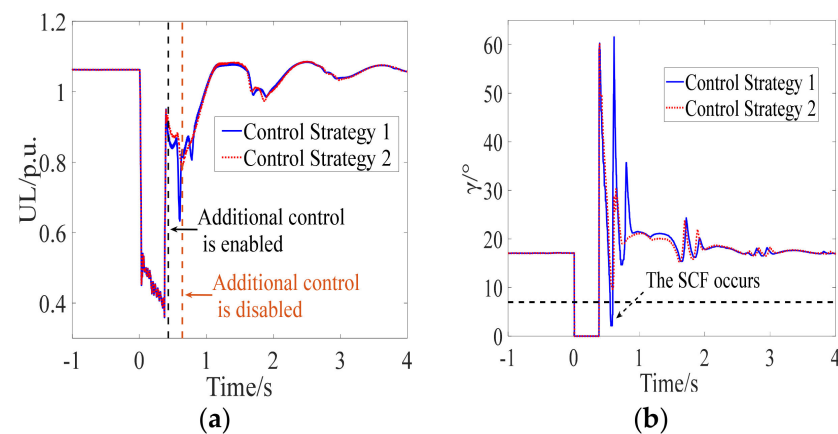


Figure 14. Cont.

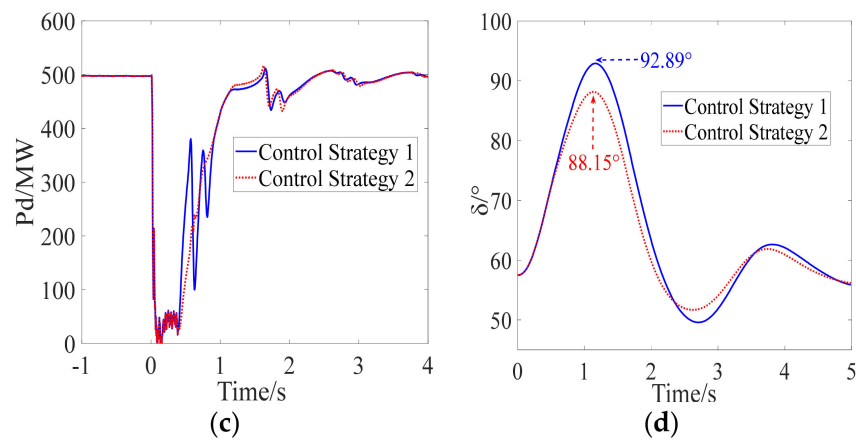


Figure 14. Simulation results of Scenario 2. (a) Inverter bus voltage, (b) extinction angle, (c) DC power, (d) relative rotor angle.

5.2. Comparative Analysis with Different Fault Types and Locations

The definition of robustness is that the control strategy has the ability to maintain a certain level of performance under uncertain disturbances. In order to investigate the robustness of the proposed control strategy, at different buses in the test power system shown in Figure 12, different types of AC faults were set near the inverter station, where the first CF caused by the AC fault was simulated. The fault duration was set to be long enough to cause an SCF in the DC system during the recovery after the clearance of the AC fault, and CS-1 and CS-2 were employed by the DC control system. The results are given in Table 1.

Table 1. Comparison of simulation results by different control strategies in different scenarios.

Fault Type	Fault Location	Fault Duration/s	Control Strategy 1		Control Strategy 2	
			SCF	MRRRA/°	SCF	Relative MRRRA/°
$f^{(1)}$	17	0.36	Y	92.89	N	88.15
	25% of l_1	0.36	Y	90.23	N	86.56
	50% of l_1	0.36	Y	90.27	N	85.87
	25% of l_2	0.40	Y	94.68	N	91.56
$f^{(1,1)}$	3	0.21	Y	86.31	N	81.61
	17	0.22	Y	90.87	N	85.95
	18	0.23	Y	89.47	N	84.30
	27	0.20	Y	88.78	N	84.52
$f^{(3)}$	3	0.16	Y	86.74	N	80.91
	17	0.17	Y	89.88	N	85.13
	18	0.18	Y	89.81	N	84.90
	27	0.15	Y	87.07	N	82.62

Note that l_1 and l_2 represent the AC transmission lines between buses 17–18 and buses 17–27, respectively.

Compared with the simulation results of the DC control system that adopted CS-1 in different scenarios, the occurrence of an SCF was prevented, demonstrating the robustness of the proposed control strategy. Due to the fact that the severe fluctuation in DC power was avoided, the maximum relative rotor angle of the post-fault sending-end power system when the DC control system adopted CS-2 is lower than that of the post-fault sending-end power system when the DC control system adopted CS-1, indicating an improvement in the transient stability margin of the sending-end power system when the DC control system adopted CS-2.

5.3. Comparative Analysis with Different SCRs

In addition, different types of AC faults were set at Bus-17 in the receiving-end system with different SCRs (high-SCR power systems, $SCR > 3$; low-SCR power systems,

$SCR \leq 3$) [32]. The fault duration was set to be long enough to cause an SCF in the DC system during the recovery after the clearance of the AC fault, and CS-1 and CS-2 were employed by the DC control system. The simulation results are given in Table 2.

Table 2. Comparison of simulation results by different control strategies at different SCRs.

SCR	Fault Type	Fault Duration/s	Control Strategy 1		Control Strategy 2	
			SCF	MRRRA/ $^{\circ}$	SCF	MRRRA/ $^{\circ}$
2.75	$f^{(1)}$	0.18	Y	88.72	N	81.35
	$f^{(1,1)}$	0.12	Y	87.84	N	80.87
	$f^{(3)}$	0.09	Y	87.84	N	80.97
3.36	$f^{(1)}$	0.20	Y	87.28	N	81.79
	$f^{(1,1)}$	0.13	Y	89.61	N	82.48
	$f^{(3)}$	0.10	Y	88.91	N	82.96
4.00	$f^{(1)}$	0.36	Y	92.89	N	88.15
	$f^{(1,1)}$	0.22	Y	90.87	N	85.95
	$f^{(3)}$	0.17	Y	89.88	N	85.13

Compared with the simulation results of the DC control system that adopted CS-1 in the receiving-end system with different SCRs, the occurrence of an SCF was prevented, and the transient stability margin of the sending-end power system was improved when the DC control system adopted CS-2, validating the robustness of the proposed control strategy.

5.4. Discussion

Although the electromechanical model is able to characterize the dynamics of synchronous generators, the electromagnetic model of the AC system was also employed to investigate the effectiveness and robustness of the proposed control strategy. The full electromagnetic model of the IEEE 39-bus test power system integrated with LCC-HVDC was built on ETSDAC. The simulation time step of ETSDAC was 50 μ s, and CS-1 and CS-2 were employed by the DC control system in the following scenarios. Due to the phase difference between the primary and secondary sides of the transformer, the steady-state rotor angles of the generators in the full electromagnetic model were different from those in the hybrid electromechanical–electromagnetic model.

Scenario 1: A three-phase short circuit fault is set at Bus-17, which starts at $t = 0$ s and lasts for 0.17 s.

As shown in Figure 15a,b, the occurrence of the AC fault causes the first CF of LCC-HVDC. After the clearance of the AC fault, it can be seen from the blue solid lines given in Figure 15a,b that an SCF occurs during the recovery when the transient stability of the post-fault receiving-end power system seriously deteriorates, demonstrating the correctness of the mechanism analysis of SCFs as affected by transient stability. When CS-2 is adopted by the DC control system, the SCF is prevented from occurring during the recovery, indicating the effectiveness of the proposed control strategy. In addition, as shown by the red dotted line in Figure 15c, the recovery characteristic of the DC power is improved due to the fact that the SCF had been prevented. Consequently, the maximum relative rotor angle of the post-fault sending-end power system when the DC control system adopted CS-2 is smaller than that of the post-fault sending-end power system when the DC control system adopted CS-1 as shown in Figure 15d. The effectiveness of the proposed control strategy is confirmed by the simulation results.

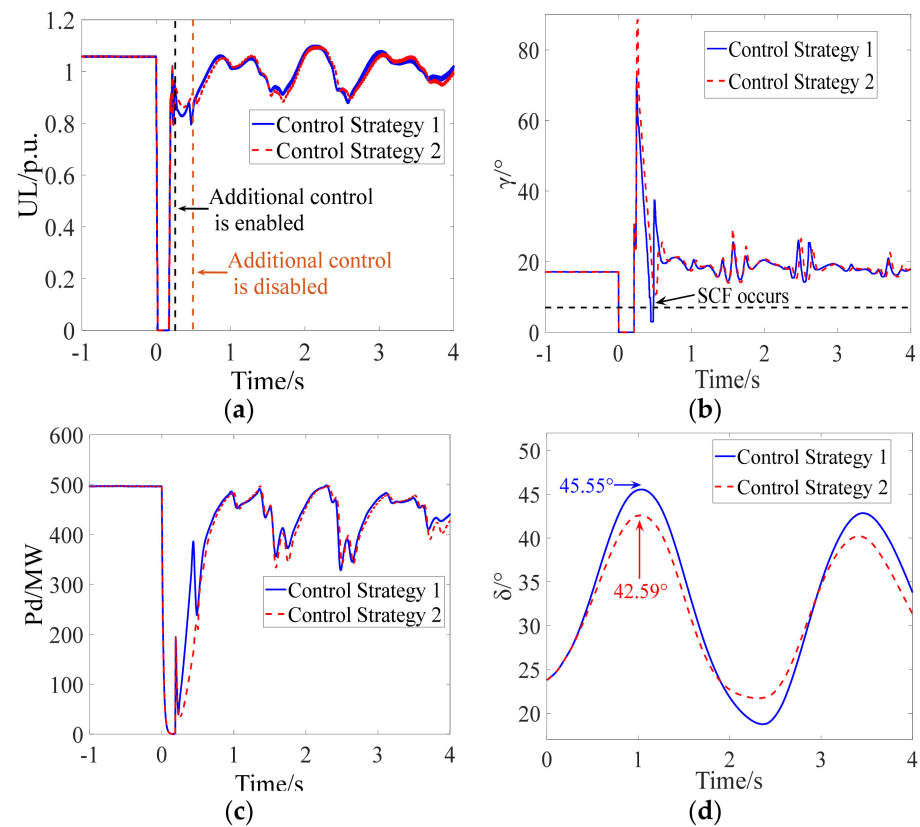


Figure 15. Simulation results of Scenario 1. (a) Inverter bus voltage, (b) extinction angle, (c) DC power, (d) relative rotor angle.

Scenario 2: A two-phase short circuit grounding fault is set at Bus-17, which starts at $t = 0$ s and lasts for 0.22 s.

As shown in Figure 16a,b, the occurrence of the AC fault causes the first CF of LCC-HVDC. After the clearance of the AC fault, the SCF is prevented when the DC control system adopts CS-2, indicating the effectiveness of the proposed recovery speed control strategy. As shown Figure 16c, the DC power recovers steadily with the regulation of the proposed control strategy. Meanwhile, the transient stability margin of the sending-end power system is improved as shown in Figure 16d.

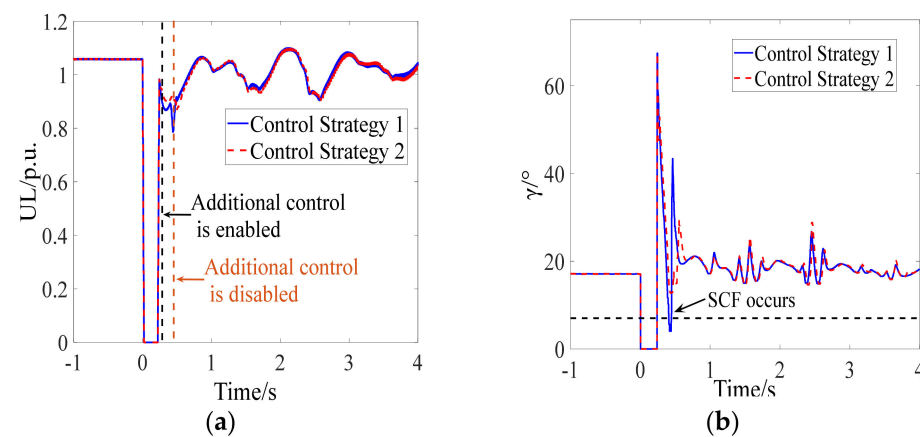


Figure 16. Cont.

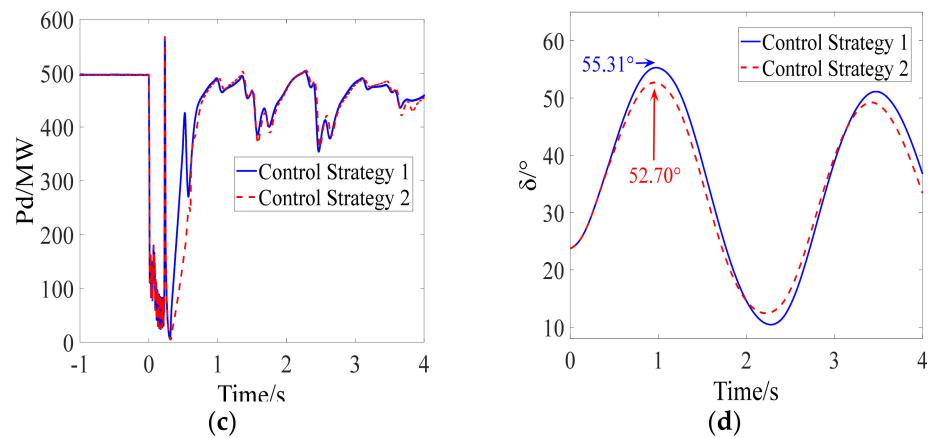


Figure 16. Simulation results of Scenario 2. (a) Inverter bus voltage, (b) extinction angle, (c) DC power, (d) relative rotor angle.

At different buses in the test power system shown in Figure 12, different types of AC faults were set near the inverter station, where the first CF caused by the AC fault was simulated. The fault duration was set to be long enough to cause an SCF in the DC system during the recovery after the clearance of the AC fault, and CS-1 and CS-2 were employed by the DC control system. The simulation results are shown in Table 3.

Table 3. Comparison of simulation results by different control strategies in the full electromagnetic model.

Fault Type	Fault Location	Fault Duration/s	Control Strategy 1		Control Strategy 2	
			SCF	MARRA/°	SCF	MARRA/°
$f^{(1)}$	17	0.50	Y	34.59	N	32.60
	10% of l_1	0.55	Y	51.36	N	48.36
	5% of l_2	0.62	Y	52.90	N	49.84
$f^{(1,1)}$	17	0.22	Y	55.31	N	52.70
	18	0.25	Y	60.00	N	56.73
	27	0.24	Y	58.74	N	56.15
$f^{(3)}$	17	0.17	Y	45.55	N	42.59
	18	0.18	Y	54.94	N	48.19
	27	0.15	Y	48.81	N	45.47

Note that l_1 and l_2 represent the AC transmission lines between buses 17–18 and buses 17–27, respectively.

Compared with the simulation results of the DC control system that adopted CS-1 in the different scenarios, the occurrence of the SCF was prevented, and the transient stability margin of the sending-end power system was improved when the DC control system adopted CS-2, validating the effectiveness and robustness of proposed control strategy.

Compared with the simulation results when the DC system adopted the electromagnetic model and the AC system adopted the electromechanical model or the electromagnetic model in the test power system, the proposed DC power recovery speed control strategy was able to prevent the occurrence of a Category 2 SCF. Moreover, the transient stability of the post-fault sending-end power system was improved due to the fact that the severe DC power fluctuation caused by the SCF had been avoided. Therefore, the effectiveness and robustness of the proposed control strategy are verified.

6. Conclusions

In this study, the mechanism of an SCF as affected by transient stability was analyzed, and a DC power recovery speed control strategy is presented as an additional form of control to prevent the occurrence of an SCF. In addition, the transient stability of the sending-end power system was improved due to the fact that the severe DC power fluctuation

caused by the SCF was avoided. Therefore, the safe and stable operation of the post-fault LCC-HVDC and AC/DC hybrid power system is guaranteed.

The dynamic interaction characteristics between the AC system and the DC system were investigated by modeling the sending-end and receiving-end power systems as synchronous generators instead of ideal voltage sources. It was found that an SCF will occur during the recovery after the clearance of the AC fault on the condition that the transient stability of the receiving-end power system has seriously deteriorated, and the recovery speed of the DC system should be limited in order to prevent its occurrence.

A risk assessment index for SCF was deduced based on a quasi-steady-state model of the DC system, a DC power recovery model was established based on the ramp function, and the impact of DC controller parameters on the DC power recovery speed was analyzed. Then, the DC power recovery speed control strategy was used to limit the recovery speed by modifying the output DC current order to prevent the occurrence of an SCF when there is a risk that one will occur during the recovery after the clearance of the AC fault.

In the proposed control strategy, the DC power recovery speed is limited by modifying the output DC current order I_{olim} to $I'_{olim} = \zeta_2 I_{olim}$. Here, ζ_2 is a constant parameter, which could be further optimized to be an adaptive parameter in future work. Based on the premise that the occurrence of SCFs can be prevented, the value of parameter ζ_2 should be as large as possible, which represents a higher DC power recovery speed and will further increase the transient stability of the post-fault AC/DC hybrid power system.

Author Contributions: Conceptualization, T.W.; methodology, T.W.; software, B.Z.; validation, Z.W.; formal analysis, B.Z.; investigation, B.Z.; resources, T.W. and Z.W.; data curation, J.H.; writing—original draft preparation, B.Z.; writing—review and editing, B.Z.; visualization, J.H.; supervision, T.W. and Z.W.; project administration, Z.W.; funding acquisition, Z.W. All authors have read and agreed to the published version of the manuscript.

Funding: This research received no external funding.

Conflicts of Interest: The authors declare no conflict of interest.

References

- Agrebi, H.; Benhadj, N.; Chaieb, M.; Sher, F.; Amami, R.; Neji, R.; Mansfield, N. Integrated optimal design of permanent magnet synchronous generator for smart wind turbine using genetic algorithm. *Energies* **2021**, *14*, 4642. [\[CrossRef\]](#)
- Khzouz, M.; Gkanas, E.I.; Shao, J.; Sher, F.; Beherskyi, D.; El-Kharouf, A.; Al Qubeissi, M. Life cycle costing analysis: Tools and applications for determining hydrogen production cost for fuel cell vehicle technology. *Energies* **2020**, *13*, 3783. [\[CrossRef\]](#)
- Shu, Y.; Chen, G.; Yu, Z.; Zhang, J.; Wang, C.; Zheng, C. Characteristic analysis of UHVAC/DC hybrid power grids and construction of power system protection. *CSEE J. Power Energy Syst.* **2017**, *3*, 325–333. [\[CrossRef\]](#)
- Sher, F.; Chen, S.; Raza, A.; Rasheed, T.; Erten, B. Novel strategies to reduce engine emissions and improve energy efficiency in hybrid vehicles. *Clean. Eng. Technol.* **2021**, *2021*, 100074. [\[CrossRef\]](#)
- Lu, J.; Yuan, X.; Hu, J.; Zhang, M.; Yuan, H. Motion equation modeling of LCC-HVDC stations for analyzing DC and AC network interactions. *IEEE Trans. Power Deliv.* **2020**, *35*, 1563–1574. [\[CrossRef\]](#)
- Xiao, H.; Li, Y.; Gole, A.M.; Duan, X. Computationally efficient and accurate approach for commutation failure risk areas identification in multi-infeed LCC-HVDC systems. *IEEE Trans. Power Electron.* **2020**, *35*, 5238–5253. [\[CrossRef\]](#)
- Mirsaeidi, S.; Dong, X. An enhanced strategy to inhibit commutation failure in line-commutated converters. *IEEE Trans. Ind. Electron.* **2020**, *67*, 340–349. [\[CrossRef\]](#)
- Guo, C.; Liu, Y.; Zhao, C.; Wei, X.; Xu, W. Power component fault detection method and improved current order limiter control for commutation failure mitigation in HVDC. *IEEE Trans. Power Deliv.* **2015**, *30*, 1585–1593. [\[CrossRef\]](#)
- Tu, J.; Pan, Y.; Zhang, J.; Jia, J.; Qin, X.; Yi, J. Study on the stability mechanism of the sending-side three-machine-group system after multiple HVDC commutation failure. *J. Eng.* **2017**, *2017*, 1140–1145. [\[CrossRef\]](#)
- Wang, W.; Xiong, X.; Li, M.; Yu, R. A flexible control strategy to prevent sending-end power system from transient instability under HVDC repetitive commutation failures. *IEEE Trans. Power Syst.* **2020**, *35*, 4445–4458. [\[CrossRef\]](#)
- Liu, L.; Lin, S.; Liu, J.; Sun, P.; Liao, K.; Li, X.; He, Z. Analysis and prevention of subsequent commutation failures caused by improper inverter control interactions in HVDC systems. *IEEE Trans. Power Deliv.* **2020**, *35*, 2841–2852. [\[CrossRef\]](#)
- Wang, J.; Huang, M.; Fu, C.; Li, H.; Xu, S.; Li, X. A new recovery strategy of HVDC system during ac faults. *IEEE Trans. Power Deliv.* **2019**, *34*, 486–495. [\[CrossRef\]](#)
- Hu, J.; Wang, T.; Wang, Z.; Liu, J.; Bi, J. Switching System's MLE Based Transient Stability Assessment of AC/DC hybrid system considering continuous commutation failure. *IEEE Trans. Power Syst.* **2021**, *36*, 757–768. [\[CrossRef\]](#)

14. Mirsaedi, S.; Dong, X. An integrated control and protection scheme to inhibit blackouts caused by cascading fault in large-scale hybrid AC/DC power grids. *IEEE Trans. Power Electron.* **2019**, *34*, 7278–7291. [[CrossRef](#)]
15. Xie, C.; Li, F. Adaptive comprehensive auto-reclosing scheme for shunt reactor-compensated transmission lines. *IEEE Trans. Power Deliv.* **2020**, *35*, 2149–2158. [[CrossRef](#)]
16. Hong, L.; Zhou, X.; Liu, Y.; Xia, H.; Yin, H.; Chen, Y.; Zhou, L.; Xu, Q. Analysis and improvement of the multiple controller interaction in LCC-HVDC for mitigating repetitive commutation failure. *IEEE Trans. Power Deliv.* **2021**, *36*, 1982–1991. [[CrossRef](#)]
17. Ouyang, J.; Zhang, Z.; Li, M.; Pan, M.; Xiong, X.; Diao, Y. A predictive method of LCC-HVDC continuous commutation failure based on threshold commutation voltage under grid fault. *IEEE Trans. Power Syst.* **2021**, *36*, 118–126. [[CrossRef](#)]
18. Tian, D.; Xiong, X.; Xiao, C. Early Warning and Inhibition of HVDC subsequent commutation failure during recovery process under grid fault. *IEEE Trans. Power Deliv.* **2021**, *36*, 1051–1062. [[CrossRef](#)]
19. Wang, J.; Gong, Y.; Fu, C.; Wen, Z.; Wu, Q. A novel phase-locked loop for mitigating the subsequent commutation failures of LCC-HVDC systems. *IEEE Trans. Power Deliv.* **2021**, *36*, 1756–1767. [[CrossRef](#)]
20. Lu, J.; Yuan, X.; Zhang, M.; Hu, J. A supplementary control for mitigation of successive commutation failures considering the influence of PLL dynamics in LCC-HVDC systems. *CSEE J. Power Energy Syst.* **2020**, 1–8, (Early Access). [[CrossRef](#)]
21. Mirsaedi, S.; Tzelepis, D.; He, J.; Dong, X.; Said, D.M.; Booth, C. A controllable thyristor-based commutation failure inhibitor for LCC-HVDC transmission systems. *IEEE Trans. Power Electron.* **2021**, *36*, 3781–3792. [[CrossRef](#)]
22. Burr, J.; Finney, S.; Booth, C. Comparison of different technologies for improving commutation failure immunity index for LCC HVDC in weak AC systems. In Proceedings of the 11th IET International Conference on AC and DC Power Transmission, Birmingham, UK, 10–12 February 2015; pp. 1–8.
23. Yao, S.; Huang, W.; Hao, W.; Guo, W. Adaptive VDCOL control strategy for the recovery of the UHVDC SPC system. *J. Eng.* **2019**, *2019*, 1754–1758. [[CrossRef](#)]
24. Shao, Y.; Tang, Y. Fast evaluation of commutation failure risk in multi-infeed HVDC systems. *IEEE Trans. Power Syst.* **2018**, *33*, 646–653. [[CrossRef](#)]
25. Xu, Y.; Dong, Z.Y.; Zhao, J.; Xue, Y.; Hill, D.J. Trajectory sensitivity analysis on the equivalent one-machine-infinite-bus of multi-machine systems for preventive transient stability control. *IET Gener. Transm. Distrib.* **2015**, *9*, 276–286. [[CrossRef](#)]
26. Xue, Y.; Zhang, X. Reactive power and AC voltage control of LCC-HVDC system with controllable capacitors. *IEEE Trans. Power Syst.* **2017**, *32*, 753–764. [[CrossRef](#)]
27. Manitoba Hydro International Ltd. Monopole HVDC Transmission System Cigre Benchmark Example. 2012. Available online: <https://www.pscad.com/knowledge-base/article/189> (accessed on 10 January 2022).
28. Cheng, F.; Yao, L.; Xu, J. A comprehensive AC fault ride-through strategy for HVDC link with serial-connected LCC-VSC hybrid inverter. *CSEE J. Power Energy Syst.* **2022**, *8*, 175–187.
29. Wang, T.; Liu, J.; Zhu, S.; Wang, Z. Analytical on-line method of determining transient stability margin using protection information for asymmetric faults. *IET Gener. Transm. Distrib.* **2020**, *14*, 191–199. [[CrossRef](#)]
30. Hu, J.; Wang, T.; Wang, Z. Transient stability margin assessment of AC/DC hybrid system with commutation failure involved. *Int. J. Electr. Power Energy Syst.* **2021**, *131*, 107056. [[CrossRef](#)]
31. China Electric Power Research Institute. User’s Manual for ADPSS. 2021. Available online: https://download.csdn.net/download/weixin_29005971/22450129 (accessed on 10 January 2022).
32. *IEEE Std 1204-1997*; IEEE Guide for Planning DC Links Terminating at AC Locations Having Low Short-Circuit Capacities. IEEE: Piscataway, NJ, USA, 1997.